

Laminar-transitional micropipe flows: energy and exergy mechanisms based on Reynolds number, pipe diameter, surface roughness and wall heat flux

A. Alper Ozalp

Received: 20 January 2011 / Accepted: 10 June 2011 / Published online: 29 June 2011
© Springer-Verlag 2011

Abstract Energy and exergy mechanisms of laminar-transitional micropipe flows are computationally investigated by solving the variable fluid property continuity, Navier–Stokes and energy equations. Analyses are carried for wide ranges of Reynolds number ($Re = 10$ – $2,000$), micropipe diameter ($d = 0.50$ – 1.00 mm), non-dimensional surface roughness ($\varepsilon^* = 0.001$ – 0.01) and wall heat flux ($q'' = 1,000$ – $2,000$ W/m²) conditions. Computations revealed that friction coefficient (C_f) elevates with higher ε^* and Re and with lower d , where the rise of ε^* from 0.001 to 0.01 induced the C_f to increase by $0.7 \rightarrow 0.9\%$ ($d = 1.00 \rightarrow 0.50$ mm), $3.4 \rightarrow 4.2\%$, $6.6 \rightarrow 8.1\%$, $9.6 \rightarrow 11.9\%$ and $12.4 \rightarrow 15.2\%$ for $Re = 100, 500, 1,000, 1,500$ and $2,000$, respectively. Earlier transition exposed with stronger micro-structure and surface roughness at the descriptive transitional Reynolds numbers of $Re_{tra} = 1,656 \rightarrow 769$ ($\varepsilon^* = 0.001 \rightarrow 0.01$), $1,491 \rightarrow 699$ and $1,272 \rightarrow 611$ at $d = 1.00, 0.75$ and 0.50 mm; the corresponding shape factor (H) and intermittency (γ) data appear in the narrow ranges of $H = 3.135$ – 3.142 and $\gamma = 0.132$ – 0.135 . At higher Re and lower d , ε^* is determined to become more influential on the heat transfer rates, such that the $Nu_{\varepsilon^*=0.01}/Nu_{\varepsilon^*=0.001}$ ratio attains the values of $1.002 \rightarrow 1.023$ ($d = 1.00 \rightarrow 0.50$ mm), $1.012 \rightarrow 1.039$, $1.025 \rightarrow 1.056$ and $1.046 \rightarrow 1.082$ at $Re = 100, 500, 1,000$ and $2,000$. As ε^* comes out to cause minor variations in the cross-sectional thermal entropy generation rates ($S'_{\Delta T}$), q'' is confirmed to augment $S'_{\Delta T}$, where the impact becomes more pronounced at higher Re and d . Frictional entropy generation values ($S'_{\Delta P}$) are found to be motivated by lower d , higher Re and ε^* , such that the $S'_{\Delta P_{d=0.50mm}}/S'_{\Delta P_{d=1.00mm}}$ ratio is computed as

$4.0011 \rightarrow 4.0014$ ($\varepsilon^* = 0.001 \rightarrow 0.01$), $4.002 \rightarrow 4.007$, $4.006 \rightarrow 4.027$ and $4.023 \rightarrow 4.102$ at $Re = 100, 500, 1,000$ and $2,000$. As the role of q'' on total entropy generation (S') turns out to be more remarkable at higher d and lower Re , the task of ε^* becomes more sensible at higher Re .

List of symbols

a	Curve fit constants
A	Cross sectional area (m ²)
C_f	Friction coefficient
C_f^*	Normalized friction coefficient
C_p	Specific heat (J/kgK)
d	Diameter (m)
ΔT	Mean-temperature variation (K)
e	Internal energy per unit mass (J/kg)
$f_\varepsilon(z)$	Surface roughness model function
h	Convective heat transfer coefficient (W/m ² K)
H	Shape factor
k	Kinetic energy per unit mass (J/kg)
L	Pipe length (m)
\dot{m}	Mass flow rate (kg/s)
Nu	Nusselt number
P	Static pressure (Pa)
Pr	Prandtl number
q''	Surface heat flux (W/m ²)
q''_r	Radial heat flux (W/m ²)
q''_z	Axial heat flux (W/m ²)
r	Radial direction
R	Radius (m)
Re	Reynolds number
S'	Cross-sectional total entropy generation (W/mK)
$S'_{\Delta P}$	Cross-sectional frictional entropy generation (W/mK)
$S'_{\Delta T}$	Cross-sectional thermal entropy generation (W/mK)

A. A. Ozalp (✉)
Department of Mechanical Engineering, University of Uludag,
16059 Gorukle, Bursa, Turkey
e-mail: aozalp@uludag.edu.tr

t	Time (s)
T	Temperature (K)
U_z	Axial velocity (m/s)
\vec{V}	Velocity vector (m/s)
z	Axial direction

Greek symbols

ε	Roughness amplitude (mm)
ε^*	Non-dimensional surface roughness ($=\varepsilon/d$)
δ_i	Kronecker unit tensor
ϕ_{ave}	Cross-sectional average irreversibility distribution ratio
κ_f	Thermal conductivity of fluid (W/mK)
γ	Intermittency
μ	Dynamic viscosity (Pa.s)
ν	Kinematic viscosity (m^2/s)
θ	Peripheral direction
ρ	Density (kg/m^3)
τ	Shear stress (Pa)
ζ	Water properties
Ψ_{loss}	Power loss (W)
ω	Roughness period (mm)
ω'	Roughness periodicity parameter ($=\omega/\varepsilon$)

Subscripts

c	Center
ex	Exit
h	Hydraulic
in	Inlet
lam	Laminar
o	Mean
r, θ , z	Radial, peripheral, axial
s	Surface
tra	Transitional
turb	Turbulent
w	Wall

Superscripts

'''	Local rate
T	Temperature dependency

1 Introduction

The significantly expanding global industrial energy needs constituted a universal research-frame that serves all technological and scientific platforms on the basis of energy management and power supervision. The concept of energy management is in the agenda of not only worldwide applicable systems, such as heat exchangers [1], but also local prospects, as that of a particular geothermal application [2], where the transport of energy, among the independent but interacting plant components, is mostly

provided by fluid flow through pipes. Besides, the contemporary comprising focus, in the methodology of augmenting efficiency and suppressing power loss values, has recently lead to manufacturing and integration of microsystems, thus the fluid mechanics, heat transfer and thermodynamic concepts of flows, in designs involving micropiping arrangements, become crucial. In the last decade, with the progress of manufacturing technologies, applications with micro-flow strategies appear more frequently in various technological branches, such as microelectronics [3] and energy [4]. According to the available micro-flow literature, the widely accepted micropipe definition [5] is given with a hydraulic diameter of $d_h \leq 1,000 \mu\text{m}$ (1 mm); moreover both industrial and scientific experience pointed out the considerable impacts of micropipe diameter and surface roughness as structural factors, wall heat flux as thermal action and Reynolds number as flow character on the energy and exergy mechanisms of micropipe flows.

Energy features of micropipe flows were considered in the sub-headings of momentum and heat transfer characteristics and investigated by both computational and experimental means. Wu and Cheng [6] determined the rise of laminar Nusselt number and apparent friction coefficient with the increase of surface roughness and also reported more remarkable increase rates at higher Reynolds numbers. The mechanism of surface roughness provoked surface friction was studied by Guo and Li [7] who reported that frictional activity is responsible for the early transition from laminar to turbulent flow. The effects of surface roughness on pressure drop and heat transfer in circular tubes, for single-phase flow with small hydraulic diameters were studied by Kandlikar et al. [8]; they concluded that transition to turbulent flows occurs at Reynolds number values much below 2,300. Obot [5] reported that (1) onset of transition to turbulent flow in smooth microchannels does not occur if the Reynolds number is less than 1,000, (2) Nusselt number varies as the square root of the Reynolds number in laminar flow. Wall roughness effects in micropipe flows were taken into consideration by Engin et al. [9]; significant departures from the conventional laminar flow theory were their primary evaluation. Petropoulos et al. [10] carried out an experimental work, denoting the difficulties in sensitively measuring the velocity and pressure values in micropipe flows, and reported the variation of friction coefficient and pressure loss values with Reynolds number. Trapezoidal microchannels were in the theoretical and experimental focus of Renaud et al. [11]; they evaluated the grow of friction coefficient with higher Reynolds number and lower hydraulic diameter. Vicente et al. [12] experimentally investigated the laminar and transitional flows in dimpled tubes and indicated that the transition onset was at a relatively low Reynolds number of 1,400 where the roughness

induced friction factors were 10% higher than the smooth tube ones. As the significance of viscous dissipation on the temperature field and on the friction factor was studied numerically and experimentally by Koo and Kleinstreuer [13], Morini [14] worked on the role of the cross-sectional geometry on viscous dissipation and the minimum Reynolds number for which viscous dissipation effects can not be neglected. Parlak et al. [15] experimented smooth microtubes under adiabatic conditions and reported fairly good consistency between the measured data and the calculated data from Hagen–Poiseuille equation of laminar flow as long as the viscous heating effects are taken into account for micropipe diameters of $d < 100 \mu\text{m}$. The work of Celata et al. [16] described the roles of surface roughness on viscous dissipation, the resulting earlier transitional activity, augmented friction factor values and elevated head loss data. Slit type micro-channels were taken into experimental investigation by Almeida et al. [17]; their measurements for wide ranges of Reynolds number, hydraulic diameter and surface roughness proposed the systematic variation of frictional activity with micro structure and flow characteristics.

The concepts on exergy are mainly examined in terms of entropy generation; the available literature displays the 2nd law analysis through the thermal and frictional fractions as well. The effects of streamwise variation of fluid temperature and rib height to diameter ratio on the entropy production of a tubular heat exchanger with enhanced heat transfer surfaces were investigated by Zimparov [18]. Hooman [19] computationally inspected the local and overall entropy generation in a micro-duct and reported the variation of entropy generation and Bejan number with Reynolds number, wall heat flux and hydraulic diameter. In a similar work Avci and Aydin [20] as well performed 2nd law calculations in hydrodynamically and thermally fully developed micropipe flows and described the link of structural, thermal and hydraulic issues with entropy generation. For single-phase, fully developed internal laminar and turbulent flows with uniform heat flux, Ratts and Raut [21] employed the entropy generation minimization method and obtained optimal Reynolds numbers. Kotas et al. [22] validated the applicability of exergy balance, or the Gouy-Stodola theorem, to compute the loss of exergy, or process irreversibility. Sahin [23] analytically inspected the entropy generation for a fully developed laminar viscous flow in a duct subjected to constant wall temperature and determined that, the dependence of viscosity on temperature becomes essentially important in accurately determining the entropy generation; he additionally reported the promoted entropy generation due to viscous friction. The thermal design of plate heat exchanger with double-sine ducts, from the point of entropy generation and exergy utilization, was numerically performed by Ko [24]. Erbay et al. [25] numerically investigated entropy generation induced by the transient laminar forced

convection in microchannels between two parallel plates. They studied the effects of aspect ratio, Reynolds number, Prandtl number and the motion of the lower plate on the entropy generation and determined that the highest entropy generation rates, for all values of group parameters, were located on the channel walls. Parlak et al. [15] experimentally observed that the second law characteristics in the smooth micropipe distinguish substantially from the conventional theory for flows in larger tubes, where the entropy generation data are recorded to augment with higher Reynolds number and with lower micropipe diameter.

The scientifically up to date panorama of micropipe flows, the industrial prospect and its significance can evidently be inspected from the above presented past research. As the structural parameters and operational scenarios appear for wide ranges in real-time systems, the need in the identification of individual and combined parameter influences on micropipe flows become more decisive. Previously, the present author [26–28] computationally investigated the momentum transfer, heat transfer and second-law characteristics of air flow in a circular micropipe with the diameter of $d = 1.00 \text{ mm}$. The analyses were carried out in the Reynolds number and non-dimensional surface roughness ranges of $Re = 1\text{--}2,000$, $\varepsilon^* = 0.001\text{--}0.05$. The author continued his research for water flow with the Reynolds number, micropipe diameter, non-dimensional surface roughness ($\varepsilon^* = \varepsilon/d$) and wall heat flux limits of $Re = 10\text{--}2,000$, $d = 0.50\text{--}1.00 \text{ mm}$, $\varepsilon^* = 0.001\text{--}0.01$ and $q'' = 1,000\text{--}2,000 \text{ W/m}^2$. He [29] recently reported the initial finding set of his ongoing research, comprising the first and second-law characteristics of roughness induced laminar-transitional micropipe flows, for the fixed non-dimensional surface roughness condition of $\varepsilon^* = 0.001$. In the current article, the non-dimensional surface roughness values cover the entire range ($\varepsilon^* = 0.001\text{--}0.01$) of the project; the other acting parameters (Re , d and q'') are as well considered within their complete limits. Energy mechanisms are interpreted with radial velocity and temperature profiles, boundary layer parameters, friction coefficients, Nusselt numbers, frictional power loss and temperature rise values. Exergy based concepts are discussed in terms of cross-sectional thermal, frictional and total entropy generation rates and cross-sectional average irreversibility distribution ratio data.

2 Theoretical background

2.1 Micropipe and roughness

The geometric definition of the micropipe (Fig. 1a), considered in the present paper, are given in terms of its diameter (d) and length (L). The present roughness model is based on

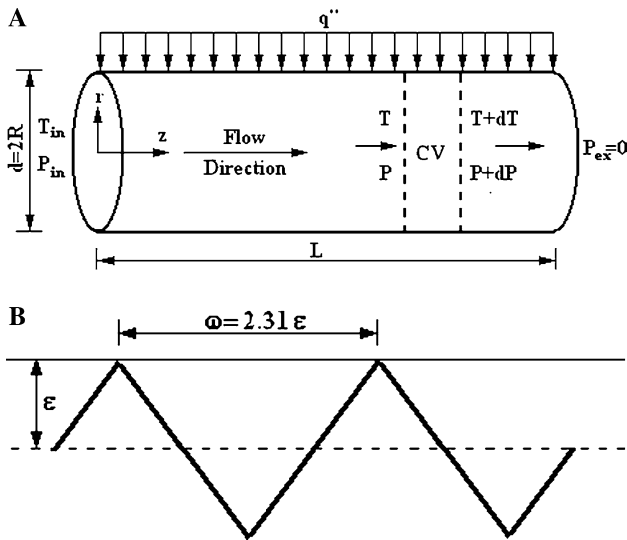


Fig. 1 a Schematic view of micropipe, b triangular surface roughness distribution

the triangular structure of Cao et al. [30] (Fig. 1b), where the roughness amplitude and period are characterized by ϵ and ω , respectively. In all computations the roughness periodicity parameter ($\omega' = \omega/\epsilon$) is kept fixed to $\omega' = 2.31$, which corresponds to equilateral triangle structure [30]. The model of Cao et al. [30] is numerically characterized by Eq. 1 with the implementation of the amplitude and period. The model function ($f_\epsilon(z)$) is repeated in the streamwise direction throughout the pipe length, where the Kronecker unit tensor (δ_i) attains the values of $\delta_i = +1$ and -1 for $0 \leq z \leq \frac{2.31}{2}\epsilon$ and $\frac{2.31}{2}\epsilon \leq z \leq 2.31\epsilon$ respectively.

$$f_\epsilon(z) = \delta_i \epsilon \left[1 - \frac{4}{2.31\epsilon} z \right] \tag{1}$$

2.2 Governing equations

It is well known that water properties like specific heat (C_p), kinematic viscosity (ν) and thermal conductivity (κ_f), are substantially dependent on temperature [31]. To comprehensively implement the property (ζ) variations with temperature into the calculations, the necessary water data of Incropera and DeWitt [31] is fitted into 6th order polynomials, which can be presented in closed form by Eq. 2a–c. The uncertainty of the fitted water data is less than 0.03% and the temperature dependency is indicated by the superscript T throughout the formulation.

$$\zeta^T = \sum_{j=0}^6 a_j T^j, \quad Re = \frac{U_o d}{\nu^T} = \frac{\rho U_o d}{\mu^T}, \tag{2a-c}$$

$$Nu = \frac{hd}{\kappa_f^T} = \frac{\partial T / \partial r|_{r=R} d}{T_s - T_o} \tag{2a-c}$$

As the average velocity of the flow at any cross-section of the pipe is denoted by U_o , the density, dynamic and kinematic viscosity of water are defined with ρ , μ and ν ($=\mu/\rho$). The surface and mean flow temperatures are denoted by T_s and T_o ; thermal conductivity and convective heat transfer coefficient are characterized by κ_f and h . Using these definitions Reynolds number and Nusselt number are given by Eq. 2a–c. Throughout the theory and the discussion sections of the paper, Reynolds and Nusselt numbers are based only on the diameter of the micropipe; thus they are interpreted solely by Re and Nu , respectively.

The flow boundary conditions are based on the facts that, on the pipe wall no-slip condition and constant heat flux exist, and flow and thermal values are maximum at the centerline. As given in Fig. 1a, at the pipe inlet, pressure and temperature values are known and the exit pressure is atmospheric. The problem considered here is steady ($\partial/\partial t = 0$), fully developed and the flow direction is coaxial with pipe centerline ($U_r = U_\theta = 0$), thus the velocity vector simplifies to $\vec{V} = U_z(r)\hat{k}$, denoting $\partial U_z / \partial \theta = 0$ and $\partial U_z / \partial z = 0$. These justifications are common in several recent numerical studies, on roughness induced flow and heat transfer investigations, like those of Engin et al. [9], Koo and Kleinstreuer [13], Ozalp [29] and Cao et al. [30]. Denoting $U_z = U_z(r)$ and $T = T(r, z)$, the boundary conditions can be summarized as follows:

$$\begin{aligned} r=R+f_\epsilon(z) &\rightarrow U_z=0 \text{ and } r=0 \rightarrow \frac{\partial U_z}{\partial r}=0 \\ r=R+f_\epsilon(z) &\rightarrow \frac{\partial T}{\partial r} = -\frac{q''_r}{\kappa_f^T} \text{ and } r=0 \rightarrow \frac{\partial T}{\partial r}=0 \\ z=0 &\rightarrow P=P_{in}, \quad T=T_{in} \text{ and } z=L \rightarrow P_{ex}=0 \text{ (Manometric)} \end{aligned} \tag{3}$$

As the internal and kinetic energy terms are defined as $e=C_p^T T$ and $k=U_z^2/2$, respectively, heat flux terms (q''_r, q''_z) are given by Eq. 4a,b. In an incompressible flow application with constant pipe diameter, the viscous stress τ_{zz} vanishes due to the unvarying local and cross-sectional average velocities ($\partial U_z / \partial z = 0$) in the flow direction; the viscous stress tensor (τ_{rz}) is given by Eq. 5.

$$q''_r = -\kappa_f^T \frac{\partial T}{\partial r}, \quad q''_z = -\kappa_f^T \frac{\partial T}{\partial z} \tag{4a, b}$$

$$\tau_{rz} = \mu^T \frac{\partial U_z}{\partial r} \tag{5}$$

For fully developed laminar incompressible flow with the above problem definitions and implementations, the continuity, momentum and energy equations are given as:

$$\frac{\partial}{\partial z} (U_z) = 0 \tag{6}$$

$$\frac{\partial P}{\partial z} = \frac{1}{r} \frac{\partial}{\partial r} (r \tau_{rz}) \tag{7}$$

$$\rho U_z \frac{\partial}{\partial z} \left(e + \frac{P}{\rho} + k \right) + \frac{1}{r} \frac{\partial}{\partial r} (r q_r'') + \frac{\partial q_z''}{\partial z} = \tau_{rz} \frac{\partial U_z}{\partial r} + U_z \left[\frac{1}{r} \frac{\partial}{\partial r} (r \tau_{rz}) \right] \tag{8}$$

The average fluid velocity and temperature, at any cross-section in the pipe, are defined as

$$U_o = \frac{2\pi \int_{r=0}^{r=R} U_z(r) r dr}{\pi R^2}, \quad T_o = \frac{2\pi \int_{r=0}^{r=R} U_z(r) C_p(r) T(r) r dr}{U_o (C_p)_o \pi R^2} \tag{9a, b}$$

and the shear stress and mass flow rate are obtained from

$$\tau = C_f \frac{1}{2} \rho U_o^2 = \mu^T \left. \frac{dU_z}{dr} \right|_{r=R}, \quad \dot{m} = \rho U_o A = \rho 2\pi \int_{r=0}^{r=R} U_z(r) r dr \tag{10a, b}$$

Entropy generation, arising from the non-equilibrium phenomenon of exchange of energy and momentum within the fluid and at the solid boundaries, is considered to be directly proportional to the lost available work by the Gouy-Stodola theorem [22]. Due to the existence of the velocity and temperature gradients in the flow volume, the volumetric entropy generation rate is positive and finite. Computation of the temperature and the velocity fields through Eqs. 6–8 on the problem domain, will produce the input data for Eq. 11a,b which defines the local rate of entropy generation per unit volume (S'''), for a one-dimensional flow and two-dimensional temperature domain for incompressible Newtonian fluid flow in cylindrical coordinates. As given in Eq. 11a,b, the local entropy generation due to finite temperature differences ($S'''_{\Delta T}$) in axial z and in radial r directions is defined by the first term on the right side of Eq. 11a,b; the second term stands for the local frictional entropy generation ($S'''_{\Delta P}$).

$$S''' = \frac{\kappa_f^T}{T^2} \left[\left(\frac{\partial T}{\partial r} \right)^2 + \left(\frac{\partial T}{\partial z} \right)^2 \right] + \frac{\mu^T}{T} \left[\left(\frac{\partial U_z}{\partial r} \right)^2 \right] \tag{11a, b}$$

$$S''' = S'''_{\Delta T} + S'''_{\Delta P}$$

As the cross-sectional frictional, thermal and total entropy generation rates can be obtained by Eq. 12a–c, Eq. 13 stands for the cross-sectional average irreversibility distribution ratio.

$$S'_{\Delta P} = 2\pi \int_{r=0}^{r=R} S'''_{\Delta P} r dr, \quad S'_{\Delta T} = 2\pi \int_{r=0}^{r=R} S'''_{\Delta T} r dr \tag{12a - c}$$

$$S' = 2\pi \int_{r=0}^{r=R} S''' r dr$$

$$\phi_{ave} = \frac{S'_{\Delta P}}{S'_{\Delta T}} \tag{13}$$

2.3 Computational method

Laminar micropipe flow with surface roughness and heat flux governs the complete equation set described in the previous section, which are highly dependent non-linear formulations, where the convergence problems and singularities are most likely to occur in the solution scheme of the sufficiently complex structure. Forward difference discretization is applied in the axial and radial directions, for the two-dimensional marching procedure. The flow domain of Fig. 1a is divided into m axial and n radial cells ($m \times n$), where the fineness of the computational grids is examined to ensure that the obtained solutions are independent of the grid employed. Since the computational findings must be independent of the employed number of cells, optimum meshing is determined by performing several successive runs; where the optimum axial and radial cell numbers are determined as $m = 500 \rightarrow 850$ and $n = 100 \rightarrow 225$ respectively, for $d = 1.00 \rightarrow 0.50$ mm. Table 1 displays a summary of these tests for the 3 micropipe diameters of $d = 1.00, 0.75$ and 0.50 mm in terms of the momentum, thermal and exergy parameters that are the primary concerns of the present research for the highest Reynolds number case of $Re = 2,000$. Since the velocity and temperature gradients are significant on the pipe walls, the 20% of the radial region, neighboring solid wall, is employed an adaptive meshing with radial-mesh width aspect ratio of $1.1 \rightarrow 1.05$ ($d = 1.00 \rightarrow 0.50$ mm). For simultaneous handling, Eqs. 6–8 need to be assembled into the 3-dimensional “Transfer Matrix”, consisting of the converted explicit forms of the principle equations. Direct Simulation Monte Carlo (DSMC) method is a utilized technique especially for internal flow applications with instabilities. The author previously applied DSMC to compressible [26–28] and incompressible [29] micro-pipe flow scenarios with surface roughness and to compressible nozzle flow problems [32]; besides Wu and Tseng [33] as well employed DSMC in a micro-scale gas dynamics domain. DSMC method can couple the influences of surface roughness and surface heat flux conditions over the meshing intervals of the flow domain. The benefits become apparent when either the initial guesses on inlet pressure and inlet velocity do not result in convergence within the implemented mesh, or if the converged solution does not point out the desired Reynolds number in the pipe. Moreover, as defined in detail by Ozalp [26–29, 32], to enable the application of different types of boundary conditions with less specific change in programming, cell-by-cell transport tracing technique is adopted to support the “Transfer Matrix” scheme and to the DSMC algorithm.

Table 1 Cell number effects on momentum, thermal and exergy parameters

d (mm)	# of cells (m × n)	C_f^* ($\varepsilon^* = 0.001 \rightarrow 0.01$)	Nu ($\varepsilon^* = 0.001 \rightarrow 0.01$)	ϕ_{ave}^{ζ} ($\varepsilon^* = 0.001 \rightarrow 0.01$)
1.00	400 × 65	1.108 → 1.186	5.75 → 5.91	11.74 → 11.82
	450 × 75	1.116 → 1.243	5.78 → 5.94	11.77 → 11.98
	475 × 90	1.188 → 1.256	5.80 → 6.04	11.80 → 12.13
	500 × 100 χ	1.119 → 1.259	5.80 → 6.06	11.81 → 12.16
0.75	500 × 100	1.124 → 1.153	6.17 → 6.51	37.21 → 38.12
	550 × 125	1.129 → 1.241	6.19 → 6.57	38.09 → 39.23
	600 × 140	1.132 → 1.279	6.24 → 6.62	39.16 → 39.92
	625 × 150 χ	1.134 → 1.283	6.25 → 6.64	39.23 → 41.01
0.50	625 × 150	1.134 → 1.208	7.04 → 7.49	231.34 → 245.17
	750 × 180	1.143 → 1.286	7.11 → 7.58	240.78 → 256.93
	825 × 215	1.149 → 1.326	7.14 → 7.71	246.41 → 264.27
	850 × 225 χ	1.151 → 1.329	7.14 → 7.72	246.74 → 264.88

χ optimum cell numbers, $\zeta q'' = 2,000 \text{ W/m}^2$

The concept of triple transport conservation is incorporated into the DSMC, which makes it possible to sensitively evaluate the balance of heat swept from the micropipe walls and the energy transferred in the flow direction and also to perform accurate simulation for inlet/exit pressure boundaries. By simultaneously conserving mass flux and boundary pressure matching within the complete mesh, thermal equilibrium is satisfied at each pressure boundary in the flow volume. Computations are based on the pre-conditions that, maximum allowable deviation of the exit pressure from the related boundary condition (Eq. 3) is less than 0.01 Pa and the convergence criteria for the mass flow rate throughout the flow volume is in the order of 0.01%. To investigate the streamwise variations of the three primary flow parameters (U, P, T), the resulting nonlinear system of equations is solved by using the Newton–Raphson method. In the case of a convergence problem, U, P and T are investigated up to the singularity point, and then the local velocity is compared with the inlet value together with the location of the singularity point with respect to the inlet and exit planes. The inlet velocity is then modified by DSMC, by considering the type of singularity, the velocity variation and the corresponding pipe length. However inlet pressure and velocity are both modified, to increase or decrease the Reynolds number of the former iteration step, in the case that the Reynolds number does not fit the required value.

3 Results and discussion

To enlighten the energy and exergy mechanisms of laminar-transitional micropipe flows and to detail the integrated affects of Reynolds number, micropipe diameter, non-

dimensional surface roughness and wall heat flux, analyses are carried out in the wide ranges of $Re = 10\text{--}2,000$, $d = 0.50\text{--}1.00 \text{ mm}$, $\varepsilon^* = 0.001\text{--}0.01$ and $q'' = 1,000\text{--}2,000 \text{ W/m}^2$. As the non-dimensional surface roughness range is in harmony with those of Engin et al. [9] ($\varepsilon^* \leq 0.08$) and Ozalp [26–29] ($\varepsilon^* = 0.001\text{--}0.05$), the considered micropipe diameter range is consistent with the microchannel definition of Obot [5] ($d \leq 1.00 \text{ mm}$). The fixed parameters of the analyses are the length of the micropipe ($L = 0.5 \text{ m}$), inlet temperature ($T_{in} = 278 \text{ K}$) and exit pressure ($P_{ex} = 0 \text{ Pa}$). Besides, to bring about applicable and rational heating, the imposed wall heat flux values are decided in conjunction with the Reynolds number and the accompanying mass flow rate ranges. Energy based concepts are discussed in terms of radial velocity and temperature profiles, boundary layer parameters, friction coefficients, Nusselt numbers, frictional power loss and temperature rise values. Exergy mechanisms are interpreted with cross-sectional thermal, frictional and total entropy generation rates and cross-sectional average irreversibility distribution ratio data.

3.1 Energy mechanisms

3.1.1 Momentum characteristics

The roles of wall roughness (ε), micropipe diameter (d) and Reynolds number (Re) on the momentum characteristics of laminar flow are presented in terms of the radial distributions of axial velocity profiles (VP) (Fig. 2), tabulated boundary layer parameters (Tables 2, 3), normalized (C_f^*) (Fig. 3) and classical friction coefficients (Table 4) and power loss (Ψ_{loss}) (Fig. 4) values. The characteristic laminar profile (Eq. 14a,b) and the modified turbulent

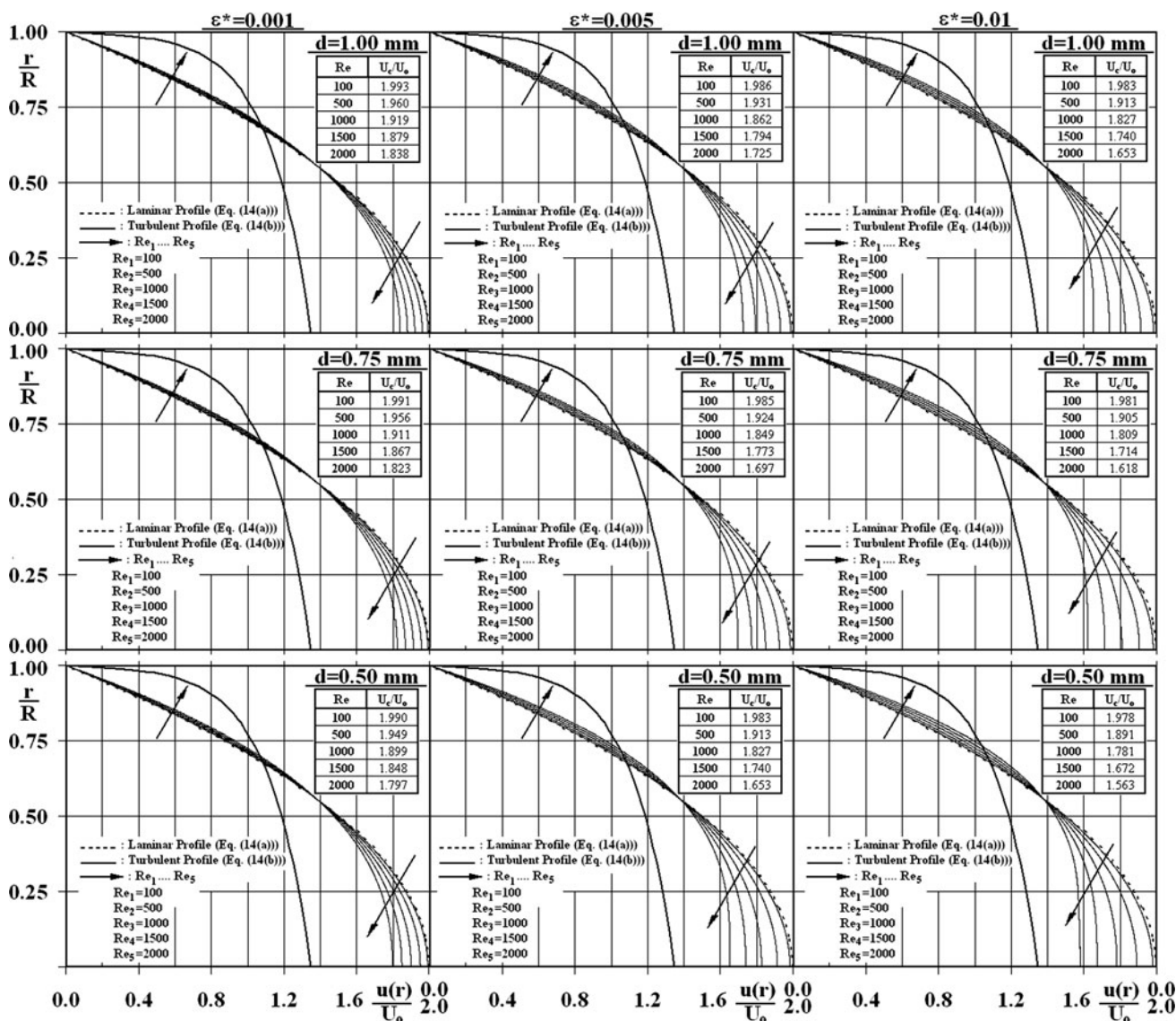


Fig. 2 Variation of radial distributions of axial velocity with d , ϵ^* and Re

logarithm law for roughness (Eq. 14a,b) (White [34]) are also displayed in Fig. 2 not only to identify the shift of the VPs from the characteristic styles of laminar and turbulent regimes but also to indicate the roles of ϵ , d and Re on the transition mechanism. Boundary layer parameters like shape factor (H) (Eq. 15a,b) and intermittency (γ) (Eq. 15a,b) [34] are integrated into the discussions to strengthen the evaluations on the onset of transition. As the laminar ($H_{lam} = 3.36$) and turbulent ($H_{turb} = 1.70$) shape factor values are computed with Eq. 15a,b, by integrating the laminar (Eq. 14a,b) and turbulent (Eq. 14a,b) profiles, the shape factor data of the transitional flows were also calculated with Eq. 15a,b, however with the computationally evaluated corresponding velocity profiles. To clarify the role of surface roughness on the frictional activity, the classical and normalized friction coefficient values are

evaluated by Eq. 16a–c [34]. Besides, numerical findings confirmed that the intensity of applied heat flux values had no influence on hydrodynamic boundary layer formation, VP distribution, C_f^* variation and Ψ_{loss} quantity; therefore the plotted velocity profiles and normalized friction coefficient data put forward the combined impacts of surface roughness, micropipe diameter and Reynolds number on the momentum characteristics.

$$\frac{U(r)}{U_0} = 2 \left[1 - \left(\frac{r}{R} \right)^2 \right], \quad \frac{U(r)}{\sqrt{\tau_w/\rho}} = 2.44 \ln \left(\frac{R-r}{\epsilon} \right) + 8.5 \tag{14a, b}$$

$$H = \frac{\int_{r=0}^{r=R} \left(1 - \frac{U(r)}{U_c} \right) r dr}{\int_{r=0}^{r=R} \frac{U(r)}{U_c} \left(1 - \frac{U(r)}{U_c} \right) r dr}, \quad \gamma = \frac{H_{lam} - H}{H_{lam} - H_{turb}} \tag{15a, b}$$

Table 2 Variation of H with d, ε^* and Re

	H					
	d = 1.00 mm		d = 0.75 mm		d = 0.50 mm	
	$\varepsilon^* = 0.001$	$\varepsilon^* = 0.01$	$\varepsilon^* = 0.001$	$\varepsilon^* = 0.01$	$\varepsilon^* = 0.001$	$\varepsilon^* = 0.01$
Re = 100	3.347	3.331	3.346	3.328	3.344	3.324
Re = 500	3.291	3.212	3.284	3.197	3.273	3.173
Re _{tra} = 611	–	–	–	–	–	3.135
Re _{tra} = 699	–	–	–	3.138	–	–
Re _{tra} = 769	–	3.139	–	–	–	–
Re = 1,000	3.224	3.080	3.211	3.056	3.190	3.018
Re _{tra} = 1,272	–	–	–	–	3.140	–
Re _{tra} = 1,491	–	–	3.142	–	–	–
Re = 1,500	3.160	2.968	3.141	2.939	3.112	2.899
Re _{tra} = 1,656	3.140	–	–	–	–	–
Re = 2,000	3.099	2.874	3.075	2.847	3.039	2.818

Table 3 Variation of γ with d, ε^* and Re

	γ					
	d = 1.00 mm		d = 0.75 mm		d = 0.50 mm	
	$\varepsilon^* = 0.001$	$\varepsilon^* = 0.01$	$\varepsilon^* = 0.001$	$\varepsilon^* = 0.01$	$\varepsilon^* = 0.001$	$\varepsilon^* = 0.01$
Re = 100	0.008	0.018	0.009	0.019	0.010	0.022
Re = 500	0.042	0.089	0.046	0.098	0.052	0.113
Re _{tra} = 611	–	–	–	–	–	0.135
Re _{tra} = 699	–	–	–	0.134	–	–
Re _{tra} = 769	–	0.133	–	–	–	–
Re = 1,000	0.082	0.168	0.090	0.183	0.102	0.206
Re _{tra} = 1,272	–	–	–	–	0.132	–
Re _{tra} = 1,491	–	–	0.132	–	–	–
Re = 1,500	0.121	0.236	0.132	0.254	0.149	0.278
Re _{tra} = 1,656	0.132	–	–	–	–	–
Re = 2,000	0.158	0.293	0.172	0.309	0.193	0.327

$$C_f = \frac{2\mu^T \left| \frac{dU}{dr} \right|_{r=R}}{\rho_o U_o^2}, \quad (C_f)_{lam} = \frac{16}{Re}, \quad C_f^* = \frac{C_f}{(C_f)_{lam}} \tag{16a - c}$$

Figure 2 demonstrates the radial distributions of axial velocity for various non-dimensional surface roughness ($\varepsilon^* = 0.001, 0.005, 0.01$), micropipe diameter ($d = 1.00, 0.75, 0.50$ mm) and Reynolds number ($Re = 100, 500, 1,000, 1,500, 2,000$) cases. Due to the insensitive impact of surface roughness on the laminar momentum mechanism of the micropipe flow, the VP of the flow scenarios at $Re = 100$ shown no inspectable deviation from the characteristic laminar profile for the complete ε^* and d ranges taken into consideration. The boundary layer parameters sensitively points out the very minor shifts from the laminar

behavior with $H = 3.347 \rightarrow 3.331$ & $\gamma = 0.008 \rightarrow 0.018$ ($\varepsilon^* = 0.001 \rightarrow 0.01$), $H = 3.346 \rightarrow 3.328$ & $\gamma = 0.009 \rightarrow 0.019$ and $H = 3.344 \rightarrow 3.324$ & $\gamma = 0.010 \rightarrow 0.022$ for $d = 1.00, 0.75$ and 0.50 mm respectively (Tables 2, 3). With the increase of Reynolds number, VPs are more apparently affected by roughness and diameter. The lowest surface roughness of $\varepsilon^* = 0.001$ result in, although poorer but identifiable, variations in the flow domain at $Re = 500$, where the impact becomes more detectable at lower d with the interpreting data of $H = 3.291 \rightarrow 3.273$ & $\gamma = 0.042 \rightarrow 0.052$ ($d = 1.00 \rightarrow 0.50$ mm). On the other hand, due to its direct contribution on entropy generation and irreversibility distribution ratio (ϕ_{ave} —Eq. 13), the friction coefficient based viscous actions of the flow become more meaningful. Figure 3 (C_f^*) and Table 4 (C_f) point out that the frictional features of the flow are enhanced at higher ε^* . As C_f

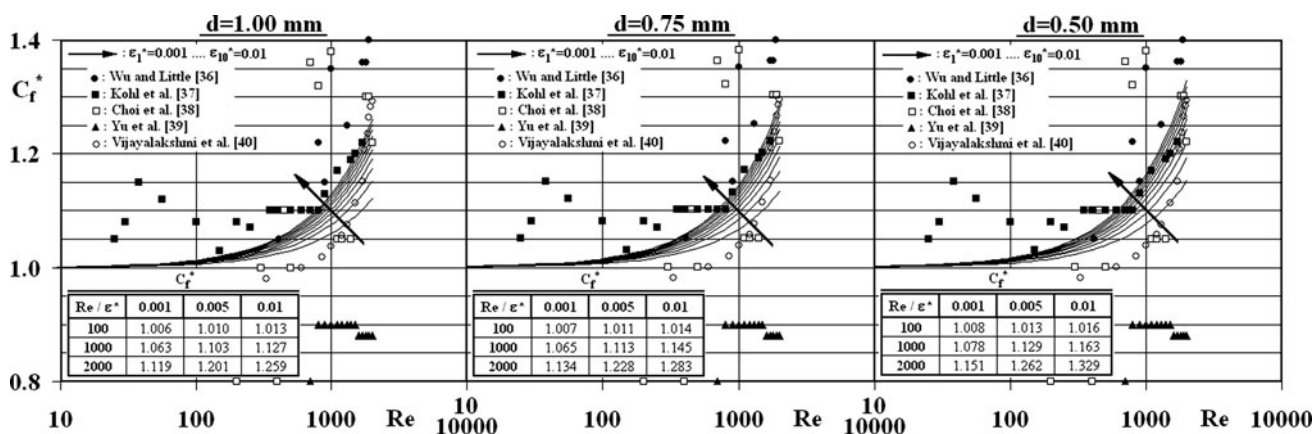
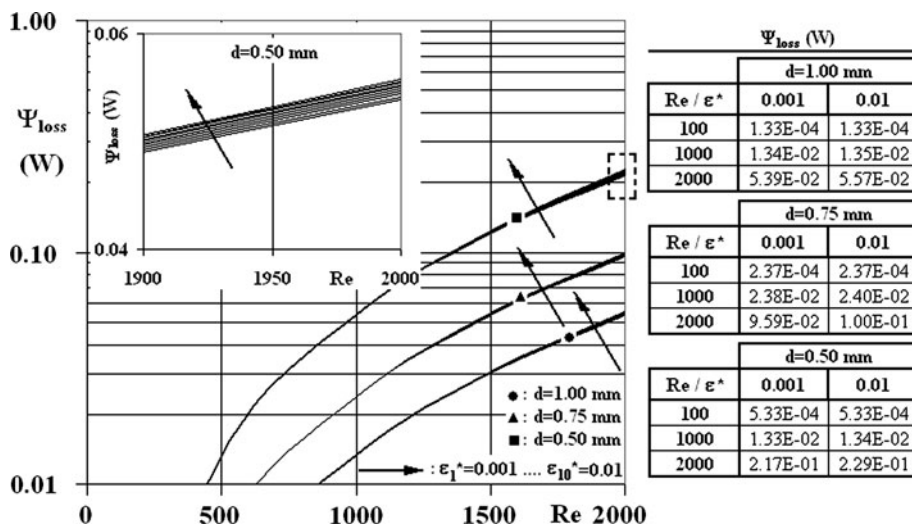


Fig. 3 Variation of C_f^* with d , ε^* and Re

Table 4 Variation of C_f with d , ε^* and Re

	C_f					
	$d = 1.00 \text{ mm}$		$d = 0.75 \text{ mm}$		$d = 0.50 \text{ mm}$	
	$\varepsilon^* = 0.001$	$\varepsilon^* = 0.01$	$\varepsilon^* = 0.001$	$\varepsilon^* = 0.01$	$\varepsilon^* = 0.001$	$\varepsilon^* = 0.01$
$Re = 100$	0.16096	0.16206	0.16105	0.16227	0.16120	0.16260
$Re = 500$	0.03296	0.03408	0.03306	0.03429	0.03321	0.03462
$Re_{tra} = 611$	–	–	–	–	–	0.02881
$Re_{tra} = 699$	–	–	–	0.02518	–	–
$Re_{tra} = 769$	–	0.02289	–	–	–	–
$Re = 1,000$	0.01696	0.01808	0.01706	0.01829	0.01722	0.01862
$Re_{tra} = 1,272$	–	–	–	–	0.01337	–
$Re_{tra} = 1,491$	–	–	0.01180	–	–	–
$Re = 1,500$	0.01163	0.01275	0.01173	0.01296	0.01188	0.01329
$Re_{tra} = 1,656$	0.01062	–	–	–	–	–
$Re = 2,000$	0.00897	0.01008	0.00906	0.01029	0.00922	0.01062

Fig. 4 Variation of Ψ_{loss} with d , ε^* and Re



grows by $\sim 0.7\%$ due to the rise of ε^* from 0.001 to 0.01 at $Re = 100$ and $d = 1.00$ mm, at the same Reynolds number the raise becomes $\sim 0.9\%$ for $d = 0.50$ mm (Table 4). With the increase of Reynolds number the increase rates in C_f become stronger with the particular values of $3.4 \rightarrow 4.2\%$ ($d = 1.00 \rightarrow 0.50$ mm), $6.6 \rightarrow 8.1\%$, $9.6 \rightarrow 11.9\%$ and $12.4 \rightarrow 15.2\%$ for $Re = 500, 1,000, 1,500$ and $2,000$. Figure 3 displays that C_f^* values augment with both higher ε^* and Re and with lower d , such that as C_f^* is evaluated as $1.006 \rightarrow 1.013$ ($\varepsilon^* = 0.001 \rightarrow 0.01$), $1.030 \rightarrow 1.065$ and $1.091 \rightarrow 1.195$ for $Re = 100, 500$ and $1,500$ respectively at $d = 1.00$ mm, the corresponding values rise to $C_f^* = 1.008 \rightarrow 1.016, 1.038 \rightarrow 1.082$ and $1.114 \rightarrow 1.246$ at $d = 0.50$ mm. These evaluations clearly indicate that the impact of surface roughness becomes more pronounced at higher Reynolds numbers and lower micropipe diameters. Guo and Li [7], Engin et al. [9], Petropoulos et al. [10], Vicente et al. [12], Almeida et al. [17] and Wang et al. [35] also reported the augmenting role of roughness on friction coefficient with Reynolds number. Renaud et al. [11], Parlak et al. [15] and Almeida et al. [17] additionally shown the grow of frictional activity in micropipes with lower diameters. Moreover, Wu and Little [36], Kohl et al. [37] and Choi et al. [38] also experimentally determined elevated friction coefficients for $Re > 500$; conversely, the experimental friction factors of Yu et al. [39] were even below the laminar theory for $100 < Re < 2,000$. On the other hand, the experimental friction coefficient data of Vijayalakshmi et al. [40] ($\varepsilon^* = 0.002$) exhibited comparably sharp increase trends especially for $Re > 700$. Figure 3 demonstrates as well the dissimilar distribution of the experimental data found in the literature [36–40], which may be attributed not only to the considered micropipe diameter and roughness ranges but also to the experimentation means. Several experimental and numerical researches, focusing on the transition phenomena in internal flow problems, interrelated the transition onset with the augmentation of friction coefficient. Among them [5, 7, 8, 12, 36] recognized a 10% rise in C_f ($C_f^* = 1.1$), above the traditional laminar formula of Eq. 16a–c, as an indicator for the transitional activity. In the present analysis, for $Re < 600$, in the complete sets of ε^* (0.001–0.01) and d (1.00–0.50 mm), the C_f^* values are lower than 1.1, indicating an ongoing laminar character. In the lowest surface roughness case of $\varepsilon^* = 0.001$ the transitional Reynolds numbers emerge as $Re_{tra} \approx 1,656, 1,491$ and $1,272$ for $d = 1.00, 0.75$ and 0.50 mm; whereas the transition onset appears at the relatively lower Reynolds numbers of $Re_{tra} \approx 769, 699$ and 611 at the upper surface roughness limit ($\varepsilon^* = 0.01$) of the study. From boundary layer parameters point of view, shape factor and intermittency possess the narrow bands of $H = 3.135$ – 3.142 (Table 2) and $\gamma = 0.132$ – 0.135 (Table 3) at the transition onset. These

results not only indicate that micropipe diameter and roughness accelerates transition to lower Reynolds numbers but also put forward that transition onset can also be determined through intermittency data, where the present computations perceive the γ data of ~ 0.135 . Moreover, the determined Re_{tra} are in harmony with the results of Obot [5] ($Re_{tra} \approx 2,040$ for inconsiderable roughness), Kandlikar et al. [8] ($Re_{tra} \approx 1,700$ for $\varepsilon^* \approx 0.003$) and Wu and Little [36] ($Re_{tra} \approx 510$ – $1,170$ for a wide range of ε^*). Figure 2 additionally demonstrates the growing influence of surface roughness on the flow pattern (VPs) with lower micropipe diameter and higher Reynolds number. The gap between the U_c/U_o ratios and the traditional data of $U_c/U_o = 2.0$ (Eq. 14a,b) increases with higher ε^* and Re , and with stronger micro structure or in other words with lower d . The rise of C_f^* and γ and the accompanying fall of H and U_c/U_o are trustable indicators not only on the impact of surface roughness and micropipe diameter on VP transformation but also on the early stages of transitional character in the fluid domain in micropipe flows.

In addition to the concepts of radial distributions of axial velocity, boundary layer parameters, friction coefficient and their dependence on Reynolds number-micropipe diameter-surface roughness, the power loss (Ψ_{loss}) amount of the flow in the micropipe pipe also needs to be considered. Viscous power loss per unit volume is the last term on the right hand side of the energy equation (Eq. 8). Since flow velocity does not vary in the streamwise direction ($\partial U_z/\partial z = 0$), due to the incompressible character, viscous power loss data can be evaluated by the volumetric integral of axial velocity (U_z) and viscous shear stress (τ_{rz}) and is given in Eq. 17.

$$\Psi_{loss} = 2\pi \int_{z=0}^{z=L} \int_{r=0}^{r=R} U_z(r) \frac{1}{r} \frac{\partial}{\partial r} (r\tau_{rz}) r dr dz \quad (17)$$

Figure 4 displays the variation of Ψ_{loss} with various ε^* , d and Re cases. It can be seen that, at the lowest micropipe diameter case of $d = 0.50$ mm, Ψ_{loss} attains the highest values in the complete ε^* and Re ranges. As denoted in Fig. 3 and Table 4, frictional behavior is evaluated to grow with higher surface roughness and lower micropipe diameter, which as a consequence promotes the viscous shear stress (τ_{rz}) as well. The direct contribution of shear intensity, together with the momentum activity, structures the power loss characteristics of the micropipe flow. However, the figure additionally reveals that the variation trends of Ψ_{loss} with Re are not linear; moreover this dependence is strongly modified by the micropipe diameter as well. Numerically it can more specifically be identified that, for the $d = 1.00$ mm case the partial derivative of $\partial \Psi_{loss}/\partial Re$ attains the values of 1.33, 2.69 and $5.40 (\times 10^{-5})$ for Re of 500, 1,000 and 2,000

respectively, whereas these values rise to 2.37, 4.79 and 9.63 ($\times 10^{-5}$) for $d = 0.75$ mm and to 5.34, 10.8 and 21.8 ($\times 10^{-5}$) for $d = 0.50$ mm. It can be inspected from these figures that the status of power loss grows more rapidly with higher Reynolds number and lower micro-pipe diameter; furthermore the impact of Reynolds number, or flow velocity, becomes more pronounced at further micro levels. Figure 4 further covers information on the affects of surface roughness on power loss ratings, where the zoomed plot for the particular case of $d = 0.50$ mm clearly demonstrates the augmenting role of ε^* on Ψ_{loss} . A detailed insight on the developing mechanism of Ψ_{loss} with ε^* can be achieved by comparing the scenario based computational outputs. As the ratio of $\Psi_{\text{loss} \varepsilon^*=0.01} / \Psi_{\text{loss} \varepsilon^*=0.001}$ comes out to be 1.002, 1.009 and 1.035 for Re of 500, 1,000 and 2,000 at $d = 1.00$ mm, the proportions become 1.003, 1.011 and 1.042 at $d = 0.75$ mm and 1.004, 1.014 and 1.055 at $d = 0.50$ mm. These records indicate that the influence of surface roughness on the power loss gains strength both at higher Reynolds number and lower micro-pipe diameter; in addition the combined action of Re and d results in a synergy on the characterizing potential of ε^* on Ψ_{loss} . Koo and Kleinstreuer [13], Morini [14] and Celata et al. [16] also reported power loss due to friction in laminar flow. They indicated that, viscous dissipation is directly related with Reynolds number where they experimentally and numerically recorded exponential augmentations in energy loss due to high Re , which are completely harmony with the present evaluations on the power loss mechanism.

3.1.2 Thermal characteristics

The non-dimensional radial temperature profiles, evaluated with respect to the centerline value (T_c), of various micro-pipe diameter, surface roughness, heat flux and Reynolds number cases are displayed in Fig. 5. Temperature profile (TP) development is not only considerably subjected to the impact of energy loss (Ψ_{loss}) due to viscous dissipation on the solid walls but also noticeably depended on surface heat transfer rates. The laminar Constant Heat Flux (CHF) formula of Eq. 18 [31] is as well plotted in Fig. 5 to identify the deviation of the evaluated TPs and the CHF formula.

$$T(r) = T_s - \frac{2U_o \kappa_f^T R^2}{\rho C_p^T} \left(\frac{dT_o}{dz} \right) \left[\frac{3}{16} + \frac{1}{16} \left(\frac{r}{R} \right)^4 - \frac{1}{4} \left(\frac{r}{R} \right)^2 \right] \quad (18)$$

It can be inspected from the figure that the TPs of the flows for $d = 1.00$ mm exhibit minor deviations in the complete considered Re and ε^* ranges. In the lowest heat flux case of $q'' = 1,000$ W/m² the non-dimensional temperature gradients on the pipe-surface ($(\partial T / \partial r)_{r=R}$) come out to be independent of surface roughness and attained the values of 3.00,

2.98 and 2.90 ($\times 10^{-3}$) at $Re = 500, 1,000$ and $2,000$ respectively, whereas these values rise to 6.01, 5.99, and 5.91 ($\times 10^{-3}$) at $q'' = 2,000$ W/m². These numbers and Fig. 5 indicate that surface roughness have no sensible affect on TP formation at the upper micro-pipe diameter limit. Besides, the outcome on milder gradients at higher Reynolds numbers can be attributed to the superior heat energy carrying capacity of elevated mass flow rates, which can be balanced by lower surface heat transfer rates. Moreover, the stronger temperature gradients at higher heat flux conditions are an expected outcome and the computations indicated almost a two fold grow among the limiting heat flux scenarios. Figure 5 additionally puts forward that enhanced micro-activity at lower micro-pipe diameters bring out the role of surface roughness on the thermal characteristics. In the lowest micro-pipe diameter of $d = 0.50$ mm the non-dimensional $(\partial T / \partial r)_{r=R}$ are evaluated as $1.47 \rightarrow 1.48$ ($\times 10^{-3}$) ($\varepsilon^* = 0.001 \rightarrow 0.01$), $1.36 \rightarrow 1.40$ ($\times 10^{-3}$) and $0.98 \rightarrow 1.09$ ($\times 10^{-3}$) for $Re = 500, 1,000$ and $2,000$ respectively at $q'' = 1,000$ W/m², the corresponding values rise to $(\partial T / \partial r)_{r=R} = 2.93 \rightarrow 2.98$ ($\times 10^{-3}$), $2.82 \rightarrow 2.91$ ($\times 10^{-3}$) and $2.31 \rightarrow 2.59$ ($\times 10^{-3}$) at $q'' = 2,000$ W/m². Computations clearly point out that temperature gradients ascend with stronger roughness, which can be considered as a trustable foresight for increased heat transfer activity with ε^* , where Ozalp [28] also reported similar findings on air flow in a micro-pipe. On the other hand, contrary to the findings for the $d = 1.00$ mm pipe, the augmentation of temperature gradients among the limiting heat flux scenarios at $d = 0.50$ mm come out to be directly count on Reynolds number; such that the ratio of $(\partial T / \partial r)_{r=R, q''=2000 \text{ W/m}^2} / (\partial T / \partial r)_{r=R, q''=1000 \text{ W/m}^2}$ attains the values of $\sim 2.00, \sim 2.08$ and ~ 2.37 for $Re = 500, 1,000$ and $2,000$. This finding can scientifically be associated with the elevated Ψ_{loss} at higher Re and ε^* and lower d (Fig. 4). Ozalp and Dincer [41] as well computed stronger temperature gradients and heat transfer rates with the contraction of a conventional flow domain, where this finding enlightens the scientific association of the thermal mechanism of flows in micro and macro domains.

Computations put forward that, in the micro-pipe with the length of $L = 0.5$ m, the role of surface roughness on the mean-temperature variations ($\Delta T = T_{\text{ex}} - T_{\text{in}}$) of the laminar-transitional flow is ignorable, thus Fig. 6 presents the ΔT scheme for three micro-pipe diameter and two heat flux cases. It can be seen from the figure that the role of micro-pipe diameter on ΔT is ignorable at low Re . However the deviations become recognizable in the cases with higher Reynolds numbers where the application of stronger micro-character produces lower mean-temperature variations. The identifiable ΔT deviation due to d can be characterized by 1% shift among the two limiting d cases. Formulating the method with the formula of $\left(\frac{\Delta T_{d=1.00 \text{ mm}} - \Delta T_{d=0.50 \text{ mm}}}{\Delta T_{d=0.50 \text{ mm}}} \right) \times 100 = 1$ results in the

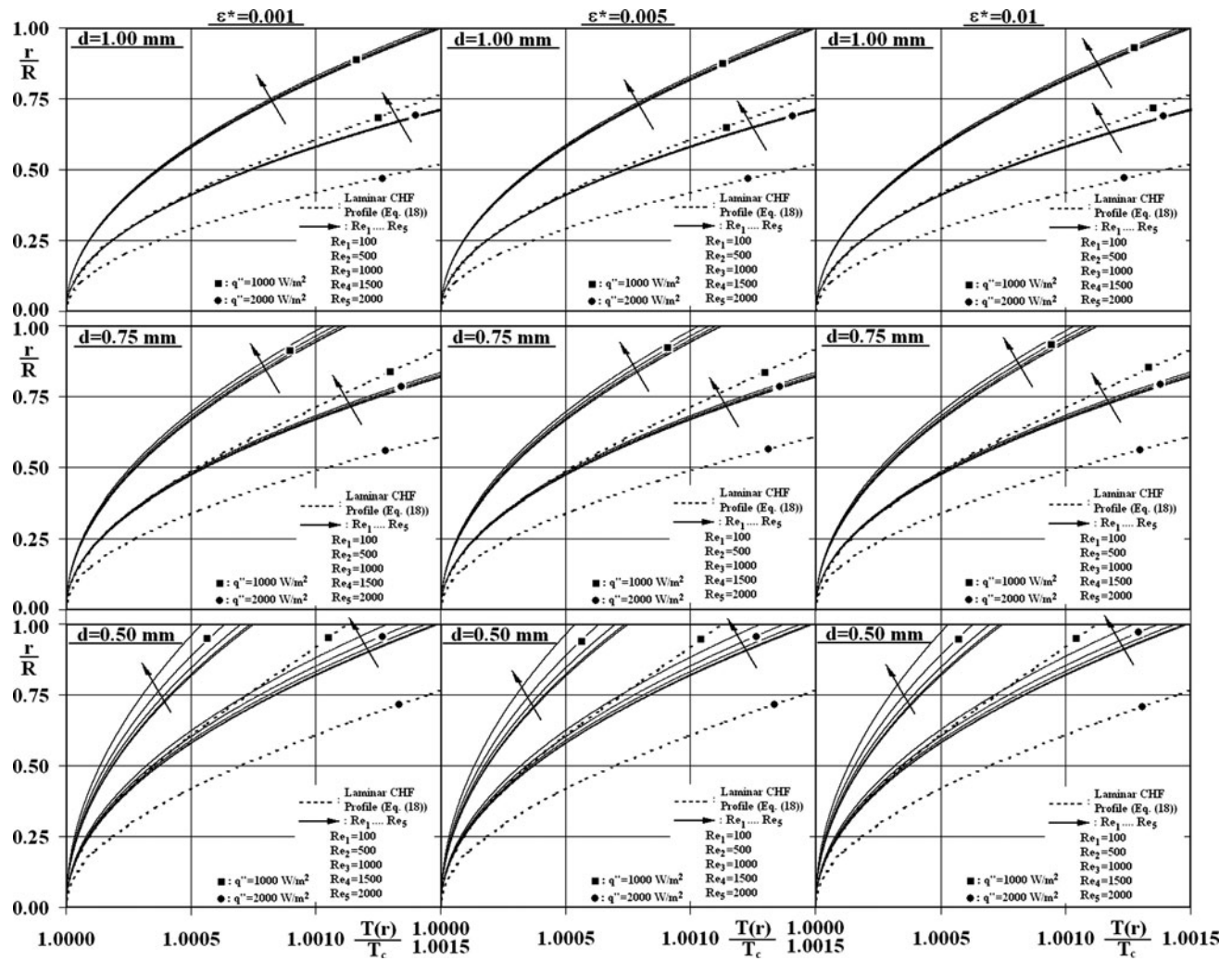


Fig. 5 Variation of radial temperature profiles with d , ε^* , Re and q''

onset Reynolds numbers of $Re = 461$ and 516 for the heat flux values of $q'' = 1,000$ and $2,000 \text{ W/m}^2$ respectively. These limits put forward that higher heat flux values delays the influential Re range of d on ΔT in laminar flow. An inverse relation, being independent of the intensity of heat flux, can as well be inspected among the mean-temperature variations and Reynolds number through Fig. 6. It can further be stated for the complete Reynolds number range that, application of higher heat flux results in augmented temperature rise values. On the other hand, computations point out that the role of heat flux on temperature rise is more remarkable at low Reynolds number cases. Moreover, it can numerically be identified that for the $q'' = 1,000 \text{ W/m}^2$ case the partial derivative of $\partial\Delta T/\partial Re$ attains the values of $-5.40 \rightarrow -5.43 (\times 10^{-3})$ ($d = 1.00 \rightarrow 0.50 \text{ mm}$), $-0.55 \rightarrow -0.58$ and $-0.24 \rightarrow -0.27$ for Re of 500, 1,000 and 2,000 respectively, whereas these values rise to $-10.80 \rightarrow -10.83 (\times 10^{-3})$, $-1.10 \rightarrow -1.13$ and

$-0.48 \rightarrow -0.51$ for $q'' = 2,000 \text{ W/m}^2$. These proportions indicate that the role of Reynolds number, thus mass flow rate, on temperature rise becomes more comprehensible in applications with higher heat flux and lower micropipe diameter. Besides, the evaluations on mean-temperature variations are completely in harmony with the temperature profile discussions (Fig. 5) and determinations on the surface temperature gradient variations with Re , d and q'' .

Combined impacts of micropipe diameter, surface roughness and Reynolds number on Nusselt number, for the ranges of $d = 1.00\text{--}0.50 \text{ mm}$, $\varepsilon^* = 0.001\text{--}0.01$ and $Re = 10\text{--}2,000$, are shown in Fig. 7, together with the traditional laminar values for constant heat flux ($Nu_{CHF} = 4.36$) and constant surface temperature ($Nu_{CST} = 3.66$). Although Wu and Little's [36] heat transfer findings are lower than the present evaluations for $Re < 1,000$, the experimental data of Obot [5] (for $Re \geq 1,000$), Kandlikar et al. [8] (for $Re \geq 500$) and Wu and Little [36] (for $Re \geq 1,000$) are

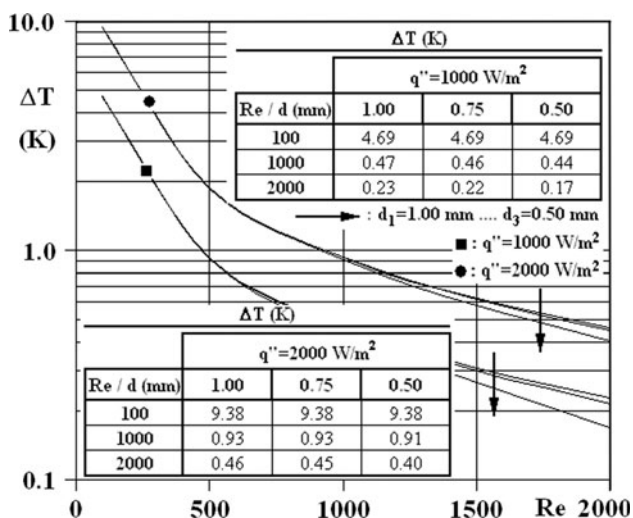


Fig. 6 Variation of ΔT with d , Re and q''

reasonably in harmony with the current numerical outputs. Computations confirmed that heat transfer rates were not affected by flow velocity, surface roughness and pipe diameter below the Reynolds number of $Re = 100$. Almost a constant Nusselt number of $Nu = 4.25$ is attained for $Re \leq 100$ for the complete d and ϵ^* ranges, which is as well within the limits of Nu_{CHF} and Nu_{CST} . Nusselt numbers are evaluated to rise with higher Reynolds numbers, where the motivation becomes more sensible with $Re > 100$. Showing parallelism with the present findings, Vicente et al. [12] also reported heat transfer augmentation with Reynolds number and recorded a constant Nusselt number of $Nu = \sim 4.36$ for $Re < 700$. Besides, Li et al.'s [42] empiric suggestion (Eq. 19a,b) not only displays the same style of the present variations but also its solution set for $d = 0.75$ mm shows close similarity with the present results of the $d = 0.50$ – 0.75 mm cases for $Re > 300$. On the other hand, the analogy of Choi et al. [38] (Eq. 19a,b), developed for the significantly low micro-pipe diameters of $d \leq 0.081$ mm,

matches with the present outputs only in the narrow Reynolds number band of $700 < Re < 900$.

$$Nu = 4.1 + \frac{0.14 * d/L * Re * Pr}{1 + 0.05 * (d/L * Re * Pr)^{2/3}} \quad (19a, b)$$

$$Nu = 0.0000972 * Re^{1.17} * Pr^{0.333}$$

Analysis further indicated that the encouraging behavior of Re on Nu is not linear and acts concurrently with d . Particularly it can more easily be clarified for the $d = 1.00$ mm case that the roughness range ($\epsilon^* = 0.001$ – 0.01) based average $Nu_{Re=100}/Nu_{Re=10}$, $Nu_{Re=500}/Nu_{Re=100}$, $Nu_{Re=1,000}/Nu_{Re=500}$ and $Nu_{Re=2,000}/Nu_{Re=1,000}$ ratios attain the values of 1.016, 1.073, 1.090 and 1.180, where these figures become $1.021 \rightarrow 1.030$, $1.094 \rightarrow 1.133$, $1.114 \rightarrow 1.156$ and $1.223 \rightarrow 1.294$ for $d = 0.75 \rightarrow 0.50$ mm. These evaluations clearly identify the growing influence of Reynolds number on Nusselt number, or on heat transfer rates, with further micro-character. Besides, comparing the Nusselt numbers evaluated at the transition Reynolds numbers (Nu_{tra}) with the laminar typical value of $Nu_{lam} = 4.25$ points out the augmentation rates of $29.8 \rightarrow 15.1\%$ ($\epsilon^* = 0.001 \rightarrow 0.01$), $33.2 \rightarrow 18.5\%$ and $41.1 \rightarrow 21.6\%$ at $d = 1.00, 0.75$ and 0.50 mm, respectively. These values put forward for the transition onset that, (1) Heat transfer activity is more potentially provoked at lower micropipe diameter cases, (2) Higher surface roughness expedite the transition mechanism substantially resulting in considerably low transitional Reynolds numbers, having comparably less excited thermal activity. It can additionally be extracted from these proportions that, for the micropipe diameter range of $d = 1.00 \rightarrow 0.50$ mm, the Nusselt numbers at the transition onset rise by a factor range of $1.30 \rightarrow 1.41$ and $1.15 \rightarrow 1.22$ at the relative roughness levels of $\epsilon^* = 0.001$ and 0.01 respectively. The augmenting role of surface roughness on heat transfer is also displayed in Fig. 7, where the mechanism is more detectable for $Re > 100$. The experimental studies of Wu and Cheng [6] and Kandlikar et al. [8] and the computational investigation of Ozalp [26] as well

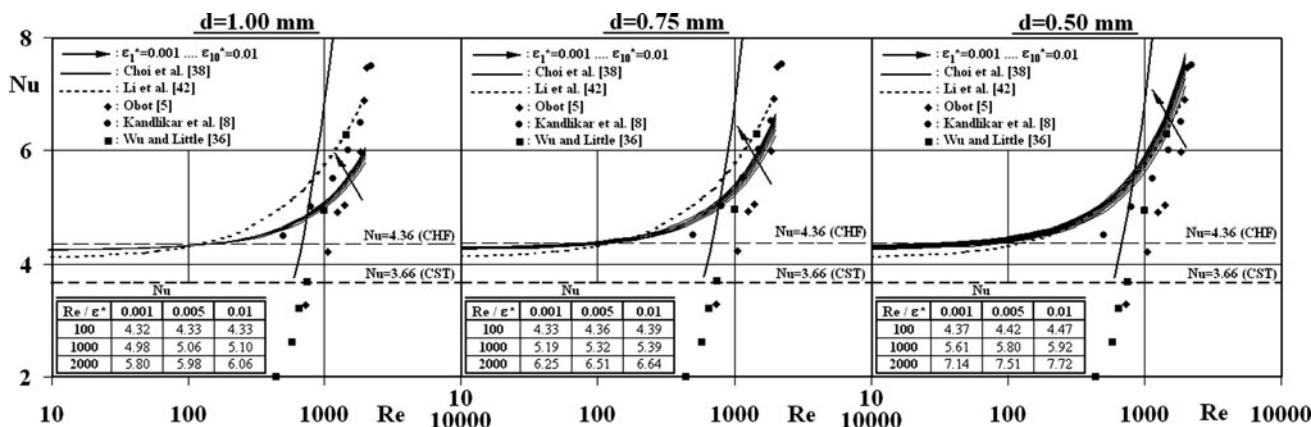


Fig. 7 Variation of Nu with d , ϵ^* and Re

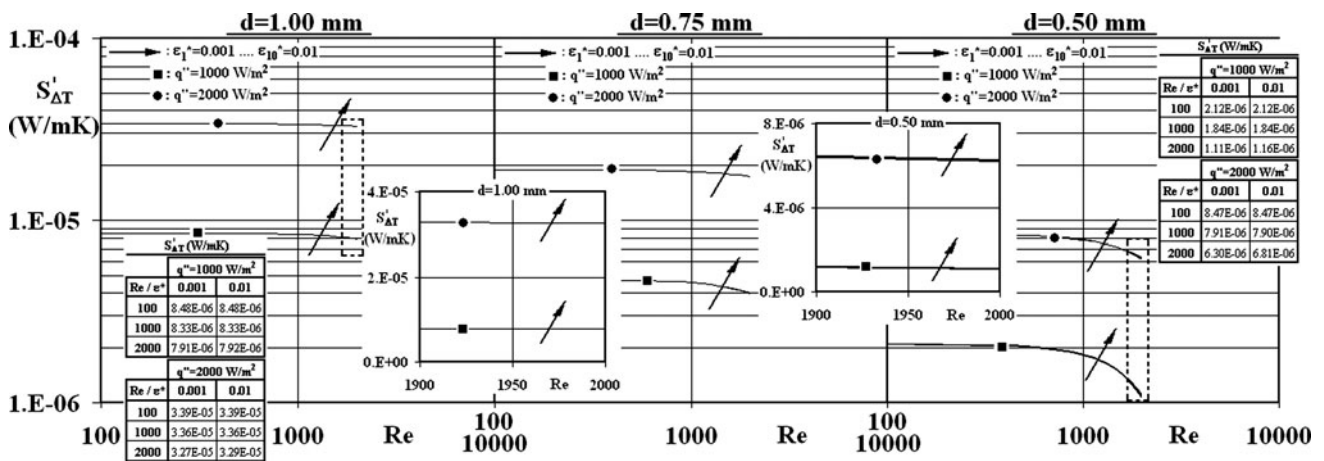


Fig. 8 Variation of $S'_{\Delta T}$ with d , ϵ^* , Re and q''

pointed out elevated heat transfer rates with surface roughness. Denoting the growing influence of surface roughness on Nusselt number at higher Reynolds numbers and lower micropipe diameters, the present calculations confirmed the $Nu_{\epsilon^*=0.01}/Nu_{\epsilon^*=0.001}$ ratios of 1.002, 1.012, 1.025 and 1.046 for $Re = 100, 500, 1,000$ and $2,000$ for the micropipe with $d = 1.00$ mm and pointed out the proportions of $1.011 \rightarrow 1.023, 1.026 \rightarrow 1.039, 1.040 \rightarrow 1.056$ and $1.062 \rightarrow 1.082$ for $d = 0.75 \rightarrow 0.50$ mm.

3.2 Exergy mechanisms

Figure 8 demonstrates the variation of cross-sectional thermal entropy generation ($S'_{\Delta T}$) for various micropipe diameter, surface roughness, Reynolds number and heat flux cases. As given in Eq. 12a–c, $S'_{\Delta T}$ is mainly characterized by the radial distributions of temperature profiles (Fig. 5) thus the impacts of d, ϵ^*, Re and q'' on $T(r)$ are significant on this issue. The elevated nature of $S'_{\Delta T}$ with higher q'' can apparently be seen from the plot, which can be attributed to the corresponding stronger temperature gradients. Computations indicated the complete surface roughness range ($\epsilon^* = 0.001\text{--}0.01$) averaged $S'_{\Delta T, q''=2000 \text{ W/m}^2}/S'_{\Delta T, q''=1000 \text{ W/m}^2}$ ratios of 3.996, 4.005, 4.031 and 4.142 at $Re = 100, 500, 1,000$ and $2,000$ for $d = 1.00$ mm; whereas these figures rise to $3.998 \rightarrow 4.001, 4.017 \rightarrow 4.068, 4.080 \rightarrow 4.298$ and $4.369 \rightarrow 5.743$ for $d = 0.75 \rightarrow 0.50$ mm. The comparably superior ratios at higher Reynolds numbers and lower micropipe diameters label the more influential scenarios of q'' on $S'_{\Delta T}$. The stronger temperature gradients in larger micropipe diameter cases (Fig. 5) caused as well additional thermal entropy generation, such that the $S'_{\Delta T, d=1.00 \text{ mm}}/S'_{\Delta T, d=0.50 \text{ mm}}$ ratios are evaluated as $4.003 \rightarrow 3.998, 4.120 \rightarrow 4.056, 4.531 \rightarrow 4.249$ and $7.003 \rightarrow 5.049$ at $Re = 100, 500, 1,000$ and $2,000$ for $q'' = 1,000 \rightarrow 2,000 \text{ W/m}^2$. It can be inspected from these

findings that the impact of micropipe diameter on thermal entropy generation becomes more pronounced at higher Reynolds number and lower heat flux cases. On the other hand, Fig. 8 displays that, when compared with the impacts of d, Re and q'' , $S'_{\Delta T}$ values are secondarily influenced by ϵ^* . The deviation of temperature profiles, due to surface roughness, were more sensible in the lowest micropipe diameter case of $d = 0.50$ mm (Fig. 5). The two zoomed plots in Fig. 8 put forward that the thermal entropy generation almost did not sense the presence of roughness in the micropipe with $d = 1.00$ mm, but the shifts among the $S'_{\Delta T}$ curves are noticeable in the flow domain with $d = 0.50$ mm. Numerically more precise detailing affirms the highest ratios for $S'_{\Delta T, \epsilon^*=0.01}/S'_{\Delta T, \epsilon^*=0.001}$ as 1.002, 1.008 and 1.044 for $d = 1.00, 0.75$ and 0.50 mm where all these evaluations correspond to the scenarios with $q'' = 1,000 \text{ W/m}^2$ and $Re = 2,000$. It can more explicitly be stated that the influence of surface roughness on thermal entropy generation becomes more significant in cases with lower surface temperature gradients.

The combined action of micropipe diameter, surface roughness and Reynolds number on the cross-sectional frictional entropy generation ($S'_{\Delta P}$) are shown in Fig. 9. As the velocity profiles are not affected from surface heat flux (Fig. 2) the $S'_{\Delta P}$ values are as well independent of q'' . In the complete micropipe diameter range considered, continuous increase trends in $S'_{\Delta P}$ with Re are evaluated. Moreover, the trends are almost linear on log–log scale; the $\partial \log S'_{\Delta P}/\partial \log Re$ attains the values of 2.008, 2.009 and 2.012 for $d = 1.00, 0.75$ and 0.50 mm, indicating the motivating role of lower micropipe diameter on the grow of frictional entropy generation with Reynolds number. Being in harmony with the findings on VP (Fig. 2) and C_f^* (Fig. 3) variation due to micropipe diameter, the $S'_{\Delta P}$ also grows in smaller micropipe scenarios, where these evaluations show harmony with the reports of Hooman [19] on elevated

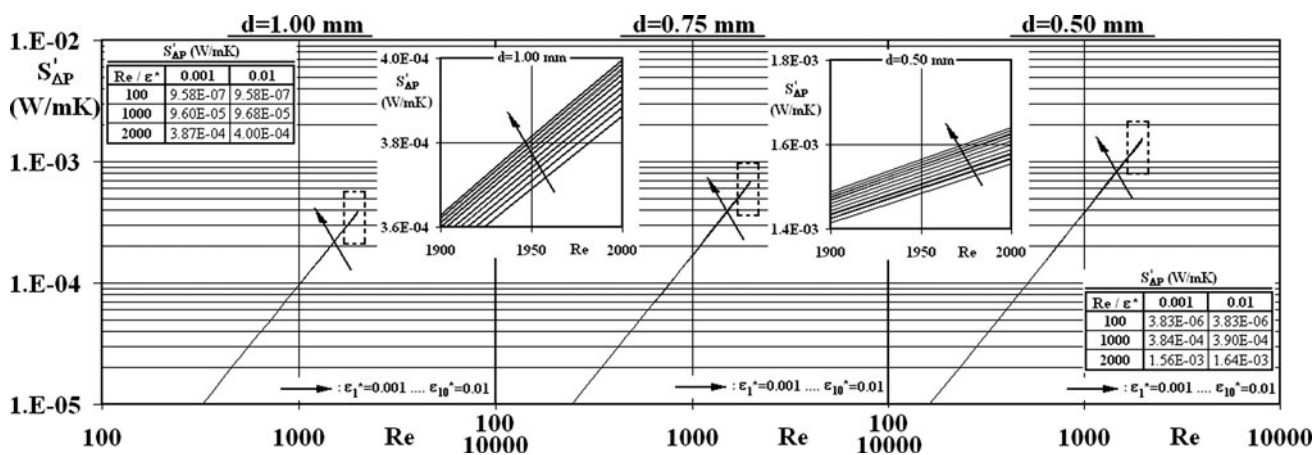


Fig. 9 Variation of $S'_{\Delta P}$ with d , ϵ^* and Re

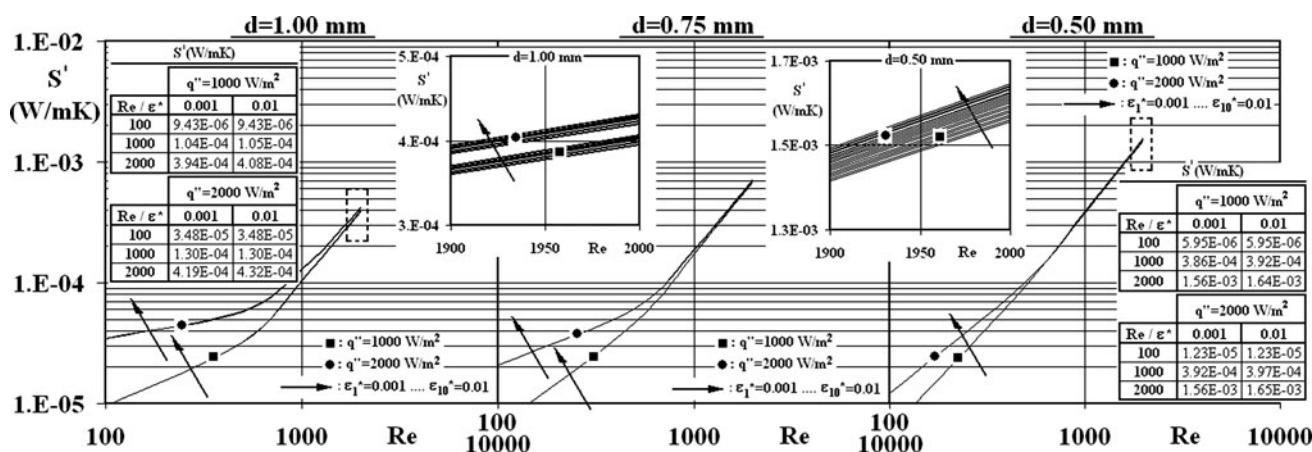


Fig. 10 Variation of S' with d , ϵ^* , Re and q''

frictional entropy generation rates with higher Reynolds number and lower micropipe diameters. The $S'_{\Delta P, d=0.50\text{mm}}/S'_{\Delta P, d=1.00\text{mm}}$ ratios are computed as $4.0011 \rightarrow 4.0014$ ($\epsilon^* = 0.001 \rightarrow 0.01$), $4.002 \rightarrow 4.007$, $4.006 \rightarrow 4.027$ and $4.023 \rightarrow 4.102$ at $Re = 100, 500, 1,000$ and $2,000$ pointing out the growing impact of enhanced micro-structure and elevated surface roughness on frictional entropy generation with Reynolds number. The zoomed plots of Fig. 9 identifies that, although minor when compared to Reynolds number and micropipe diameter, surface roughness as well promotes the frictional entropy generation. Comparing the limiting scenarios with $S'_{\Delta P, \epsilon^*=0.01}/S'_{\Delta P, \epsilon^*=0.001}$ depicts the augmentation levels of $1.000 \rightarrow 1.000$ ($d = 1.00 \rightarrow 0.50$ mm), $1.002 \rightarrow 1.003$, $1.008 \rightarrow 1.014$ and $1.034 \rightarrow 1.055$ at $Re = 100, 500, 1,000$ and $2,000$. These numerical outputs put forward that the influence of ϵ^* on $S'_{\Delta P}$ becomes more pronounced in lower d and higher Re cases.

Figure 10 exhibits the variation trends in the cross-sectional total entropy generation (S') with d , ϵ^* , Re and q'' . As the superior values with higher heat flux are due to thermal

entropy generation (Fig. 8), those values in lower micropipe diameter cases mainly depend on frictional generation rates. The plot depicts that the S' values of different q'' intensities converge with the increase of Re . The $S'_{q''=2000\text{ W/m}^2}/S'_{q''=1000\text{ W/m}^2}$ ratio appears as $3.692 \rightarrow 2.068$ ($d = 1.00 \rightarrow 0.50$ mm), $1.782 \rightarrow 1.064$, $1.241 \rightarrow 1.015$ and $1.061 \rightarrow 1.003$ at $Re = 100, 500, 1,000$ and $2,000$ respectively. These values show that heat flux is more influential on total entropy generation not only in the upper micropipe diameter limit but also at lower Reynolds numbers. The converging attitude of $S'_{q''=2000\text{ W/m}^2}$ and $S'_{q''=1000\text{ W/m}^2}$ records at high Re can evidently be seen in the zoomed plots, where the outputs become almost identical in the micropipe with $d = 0.50$ mm. Besides, similar to the findings on $S'_{\Delta T}$ and $S'_{\Delta P}$, the role of ϵ^* on S' is verified to be insignificant where the $S'_{\epsilon^*=0.01}/S'_{\epsilon^*=0.001}$ is computed to be $1.000 \rightarrow 1.000$ ($q'' = 1,000 \rightarrow 2,000$ W/m²) ($Re = 100$), $1.002 \rightarrow 1.001$ ($Re = 500$), $1.008 \rightarrow 1.006$ ($Re = 1,000$) and $1.034 \rightarrow 1.032$ ($Re = 2,000$) at $d = 1.00$ mm, whereas these numbers rise to $1.000 \rightarrow 1.000$,

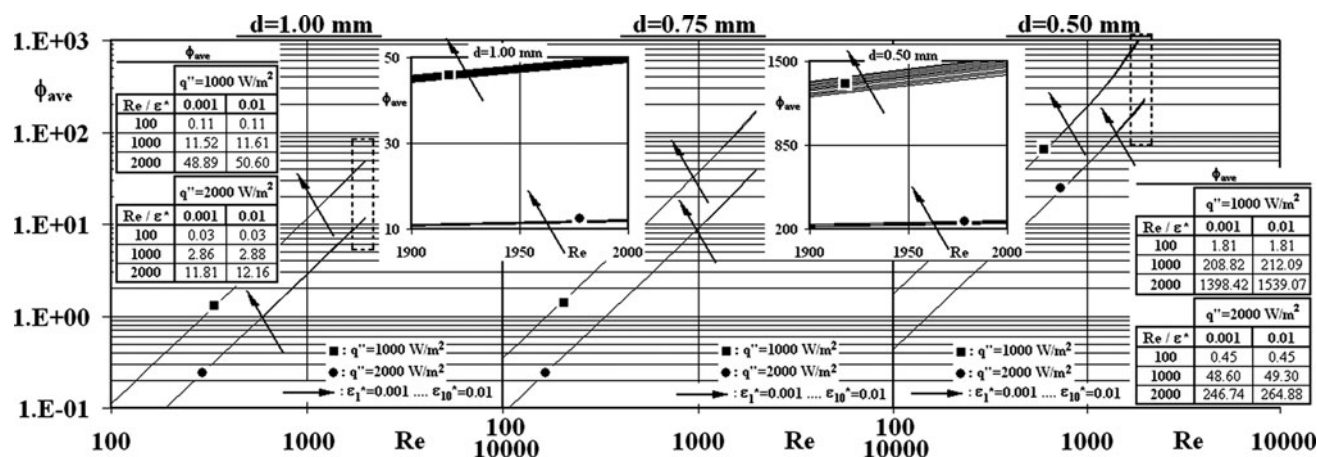


Fig. 11 Variation of ϕ_{ave} with d , ϵ^* , Re and q''

1.003 → 1.003, 1.014 → 1.013 and 1.055 → 1.054 for $d = 0.50$ mm. These evaluations put forward that the role of ϵ^* on S' resemble those of the corresponding findings for $S'_{\Delta T}$ in the low Reynolds numbers; however in the higher Reynolds number range they remind the referring figures of $S'_{\Delta P}$. This finding can be interrelated with the present determinations on (1) stronger frictional entropy generation in high fluid velocities and low micropipe diameters and (2) motivated thermal entropy generation in low Reynolds numbers, bigger micropipe diameters and intense heat flux enforcement. Similar to the present evaluations, Parlak et al. [15], Hooman [19] and Avci and Aydin [20] as well reported enhanced entropy generation rates with higher Reynolds numbers and lower micropipe diameters.

The cross-sectional average irreversibility distribution ratio data (ϕ_{ave}) of the micropipe flows for various micropipe diameter, surface roughness, Reynolds number and heat flux cases is demonstrated in Fig. 11. Due to the low $S'_{\Delta T}$ values in lower q'' intensities, the ϕ_{ave} become superior in the corresponding scenarios. The linear style of the increase trends of ϕ_{ave} with Re in log–log scale is inspectable where the $\partial \log \phi_{ave} / \partial \log Re$ are computed for the complete surface roughness range as 2.192 → 2.096 ($q'' = 1,000 \rightarrow 2,000$ W/m²), 2.057 → 2.033 and 2.027 → 2.017 for the micropipes with $d = 1.00, 0.75$ and 0.50 mm respectively. The growing influence of Reynolds number with lower heat flux and with larger diameter micropipes is identifiable from these evaluations. Besides, since $\phi_{ave} = 1$ stands for the identical $S'_{\Delta T}$ and $S'_{\Delta P}$ values, the emerging Reynolds number is as well significant from the point of energetic and exergetic issues of micropipe flows. Computations pointed out the $Re_{\phi_{ave}=1}$ values of $\sim 296 \rightarrow \sim 589$ ($q'' = 1,000 \rightarrow 2,000$ W/m²), $\sim 168 \rightarrow \sim 332$ and $\sim 80 \rightarrow \sim 150$ for $d = 1.00, 0.75$ and 0.50 mm. These figures clearly identify the encouraging action of micro-structure on frictional entropy and motivating mechanism of

heat flux on thermal entropy generation, where these outcomes are as well in harmony with the previous discussions through Figs. 8 and 9. Numerical analysis supply additional information characterizing the influence of q'' on ϕ_{ave} in different Re and d cases. The $\phi_{ave, q''=1000 \text{ W/m}^2} / \phi_{ave, q''=2000 \text{ W/m}^2}$ ratio represents the augmentation rates of 4.00 → 4.00 ($d = 1.00 \rightarrow 0.50$ mm), 4.01 → 4.07, 4.03 → 4.30 and 4.14 → 5.75 for $Re = 100, 500, 1,000$ and $2,000$, denoting the growing role of q'' on ϕ_{ave} in higher Re and lower d . Moreover, the negligible influence of surface roughness on average irreversibility distribution ratio values can be clarified by comparing the ϕ_{ave} of the limiting roughness cases. For the micropipe diameter of $d = 1.00$ mm the ratio of $\phi_{ave, \epsilon^*=0.01} / \phi_{ave, \epsilon^*=0.001}$ is calculated as 1.00 → 1.00 ($q'' = 1,000 \rightarrow 2,000$ W/m²), 1.002 → 1.002, 1.008 → 1.007 and 1.035 → 1.030 at $Re = 100, 500, 1,000$ and $2,000$, whereas these numbers rise to 1.000 → 1.000, 1.003 → 1.003, 1.016 → 1.015 and 1.101 → 1.074 for $d = 0.50$ mm. The growing treatment of ϵ^* on ϕ_{ave} with lower q'' and d and with higher Re is significant from the point of both energy and exergy mechanisms of micropipe flows, where Hooman [19] as well affirmed promoted irreversibility distribution ratio data with higher Reynolds number and lower micropipe diameters.

4 Conclusions

Combined affects of Reynolds number, micropipe diameter, surface roughness and wall heat flux on the energy and exergy mechanisms of laminar-transitional micropipe flows are numerically investigated. As momentum and thermal characteristics are presented through cross-debates by incorporating the interacting courses and parameters, discussions on exergy are structured to identify the analogous concerns and the scientific associations with the fluid

mechanics and heat transfer issues. The major outcomes of the analyses can be outlined as follows:

- Normalized friction coefficient values augment with both higher surface roughness and Reynolds number and with lower micropipe diameter. Moreover the impact of surface roughness on friction coefficient becomes more pronounced at higher Reynolds number and lower micropipe diameter, such that C_f^* is evaluated as $1.006 \rightarrow 1.013$ ($\varepsilon^* = 0.001 \rightarrow 0.01$), $1.030 \rightarrow 1.065$ and $1.091 \rightarrow 1.195$ for $Re = 100, 500$ and $1,500$ respectively at $d = 1.00$ mm; the corresponding values rise to $C_f^* = 1.008 \rightarrow 1.016$, $1.038 \rightarrow 1.082$ and $1.114 \rightarrow 1.246$ at $d = 0.50$ mm.
- Micropipe diameter and surface roughness are evaluated to accelerate transition to lower Reynolds numbers with flatter velocity profiles, lower shape factors and higher normalized friction coefficient and intermittency values.
- Higher Reynolds numbers and lower micropipe diameters cause the grow of power loss amounts; the impact of Reynolds number becomes further evident at advanced micro levels.
- The role of surface roughness on surface temperature gradients becomes more sensible at lower micropipe diameters and higher surface heat flux cases.
- As heat transfer activity is more potentially provoked at lower micropipe diameter cases, Nusselt numbers, at the transition onset, are evaluated to rise by a factor range of $1.30 \rightarrow 1.41$ ($d = 1.00 \rightarrow 0.50$ mm) and $1.15 \rightarrow 1.22$ at the relative roughness levels of $\varepsilon^* = 0.001$ and 0.01 .
- Frictional entropy generation augments with higher Reynolds number and lower micropipe diameters and is not varied by surface heat flux.
- The motivation of thermal entropy generation takes place in low Reynolds numbers, bigger micropipe diameters and intense heat flux enforcement.
- The affects of surface heat flux on total entropy generation is determined to become influential with higher micropipe diameters and at lower Reynolds numbers.
- As the impact of Reynolds number on irreversibility distribution ratio grows with lower heat flux and with larger diameter micropipes, irreversibility distribution ratio is more evidently manipulated by surface roughness with higher Reynolds number and with lower micropipe diameter and wall heat flux.
- The encouraging action of micro-structure on frictional entropy and the motivating mechanism of heat flux on thermal entropy generation are identified by the $Re_{\phi_{ave}=1}$ values of $\sim 296 \rightarrow \sim 589$ ($q'' = 1,000 \rightarrow 2,000$ W/m²), $\sim 168 \rightarrow \sim 332$ and $\sim 80 \rightarrow \sim 150$ for $d = 1.00, 0.75$ and 0.50 mm respectively.

Acknowledgments This work is supported by the Research Fund of the University of Uludag through project number: M(U)-2009/35.

References

1. Lin WW, Lee DJ (1998) Second-law analysis on wavy plate fin-and-tube heat exchangers. *J Heat Transf ASME Trans* 120:797–801. doi:10.1115/1.2824357
2. Ozgener L, Hepbasli A, Dincer I (2007) Parametric study of the effect of reference state on energy and exergy efficiencies of geothermal district heating systems (GDHS): an application of the Salihli GDHS in Turkey. *Heat Transf Eng* 28:357–364. doi:10.1080/01457630601122948
3. Petropoulos A, Kaltsas G (2010) Study and evaluation of a PCB-MEMS liquid microflow sensor. *Sensors* 10:8981–9001. doi:10.3390/s101008981
4. Granovskii M, Dincer I, Rosen MA (2006) Application of oxygen ion-conductive membranes for simultaneous electricity and hydrogen generation. *Chem Eng J* 120:193–202. doi:10.1016/j.cej.2006.01.020
5. Obot NT (2002) Toward a better understanding of friction and heat/mass transfer in microchannels—a literature review. *Microscale Thermophys Eng* 6:155–173. doi:10.1080/10893950290053295
6. Wu HY, Cheng P (2003) An experimental study of convective heat transfer in silicon microchannels with different surface conditions. *Int J Heat Mass Transf* 46:2547–2556. doi:10.1016/S0017-9310(03)00035-8
7. Guo ZY, Li ZX (2003) Size effect on microscale single-phase flow and heat transfer. *Int J Heat Mass Transf* 46:149–159. doi:10.1016/S0017-9310(02)00209-0
8. Kandlikar SG, Joshi S, Tian S (2003) Effect of surface roughness on heat transfer and fluid flow characteristics at low Reynolds numbers in small diameter tubes. *Heat Transf Eng* 24:4–16. doi:10.1080/01457630390149260
9. Engin T, Dogruer U, Evrensel C, Heavin S, Gordaninejad F (2004) Effect of wall roughness on laminar flow of Bingham plastic fluids through microtubes. *J Fluids Eng ASME Trans* 126:880–883. doi:10.1115/1.1792252
10. Petropoulos A, Kaltsas G, Randjelovic D (2010) Study of flow and pressure field in microchannels with various cross-section areas. *Microelectron Eng* 87:827–829. doi:10.1016/j.mee.2009.10.025
11. Renaud L, Malhaire C, Kleimann P (2008) Theoretical and experimental studies of microflows in silicon microchannels. *Mater Sci Eng C-Biomimetic Supramol Syst* 28:910–917. doi:10.1016/j.msec.2007.10.070
12. Vicente PG, Garcia A, Viedma A (2002) Experimental study of mixed convection and pressure drop in helically dimpled tubes for laminar and transition flow. *Int J Heat Mass Transf* 45:5091–5105. doi:10.1016/S0017-9310(02)00215-6
13. Koo J, Kleinstreuer C (2004) Viscous dissipation effects in microtubes and microchannels. *Int J Heat Mass Transf* 47:3159–3169. doi:10.1016/j.ijheatmasstransfer.2004.02.017
14. Morini GL (2005) Viscous heating in liquid flows in microchannels. *Int J Heat Mass Transf* 48:3637–3647. doi:10.1016/j.ijheattransfer.2005.01.011
15. Parlak N, Gur M, Ari V, Kucuk H, Engin T (2011) Second law analysis of water flow through smooth microtubes under adiabatic conditions. *Exp Thermal Fluid Sci* 35:60–67. doi:10.1016/j.expthermflusci.2010.08.006
16. Celata GP, Morini GL, Marconi V, McPhail SJ, Zummo G (2006) Using viscous heating to determine the friction factor in

- microchannels—an experimental validation. *Exp Thermal Fluid Sci* 30:725–731. doi:[10.1016/j.exthermflusci.2006.03.002](https://doi.org/10.1016/j.exthermflusci.2006.03.002)
17. Almeida A, Geraldes V, Semiao V (2010) Microflow hydrodynamics in slits: effects of the walls relative roughness and spacer inter-filaments distance. *Chem Eng Sci* 65:3660–3670. doi:[10.1016/j.ces.2010.03.006](https://doi.org/10.1016/j.ces.2010.03.006)
 18. Zimparov V (2000) Extended performance evaluation criteria for enhanced heat transfer surfaces: heat transfer through ducts with constant wall temperature. *Int J Heat Mass Transf* 43:3137–3155. doi:[10.1016/S0017-9310\(99\)00317-8](https://doi.org/10.1016/S0017-9310(99)00317-8)
 19. Hooman K (2008) Heat transfer and entropy generation for forced convection through a microduct of rectangular cross-section: effects of velocity slip, temperature jump, and duct geometry. *Int Commun Heat Mass Transf* 9:1065–1068. doi:[10.1016/j.icheatmasstransfer.2008.05.015](https://doi.org/10.1016/j.icheatmasstransfer.2008.05.015)
 20. Avci M, Aydin O (2007) Second-law analysis of heat and fluid flow in microscale geometries. *Int J Exergy* 4:286–301. doi:[10.1504/IJEX.2007.013395](https://doi.org/10.1504/IJEX.2007.013395)
 21. Ratts EB, Raut AG (2004) Entropy generation minimization of fully developed internal flow with constant heat flux. *J Heat Transf ASME Trans* 126:656–659. doi:[10.1115/1.1777585](https://doi.org/10.1115/1.1777585)
 22. Kotas TJ, Mayhew YR, Raichura RC (1995) Nomenclature for exergy analysis. *Proc Inst Mech Eng Part A* 209:275–280. doi:[10.1243/PIME_PROC_1995_209_006_01](https://doi.org/10.1243/PIME_PROC_1995_209_006_01)
 23. Sahin AZ (1998) Second-law analysis of laminar viscous flow through a duct subjected to constant wall temperature. *J Heat Transf ASME Trans* 120:77–83. doi:[10.1115/1.2830068](https://doi.org/10.1115/1.2830068)
 24. Ko TH (2006) Numerical analysis of entropy generation and optimal Reynolds number for developing laminar forced convection in double-sine ducts with various aspect ratios. *Int J Heat Mass Transf* 49:718–726. doi:[10.1016/j.ijheatmasstransfer.2005.08.023](https://doi.org/10.1016/j.ijheatmasstransfer.2005.08.023)
 25. Erbay LB, Yalcin MM, Ercan MS (2007) Entropy generation in parallel plate microchannels. *Heat Mass Transf* 43:729–739. doi:[10.1007/s00231-006-0164-0](https://doi.org/10.1007/s00231-006-0164-0)
 26. Ozalp AA (2008) Roughness induced forced convective laminar-transitional micropipe flow: energy and exergy analysis. *Heat Mass Transf* 45:31–46. doi:[10.1007/s00231-008-0407-3](https://doi.org/10.1007/s00231-008-0407-3)
 27. Ozalp AA (2009) Entropy analysis of laminar-forced convection in a pipe with wall roughness. *Int J Exergy* 6:249–275. doi:[10.1504/IJEX.2009.024001](https://doi.org/10.1504/IJEX.2009.024001)
 28. Ozalp AA (2009) 1st and 2nd law characteristics in a micropipe: integrated effects of surface roughness, heat flux and Reynolds number. *Heat Transf Eng* 30:973–987. doi:[10.1080/01457630902837467](https://doi.org/10.1080/01457630902837467)
 29. Ozalp AA (2010) Combined effects of pipe diameter, Reynolds number and wall heat flux and on flow, heat transfer and second-law characteristics of laminar-transitional micropipe flows. *Entropy* 12:445–479. doi:[10.3390/e12030445](https://doi.org/10.3390/e12030445)
 30. Cao BY, Chen M, Guo ZY (2006) Effect of surface roughness on gas flow in microchannels by molecular dynamics simulation. *Int J Eng Sci* 44:927–937. doi:[10.1016/j.ijengsci.2006.06.005](https://doi.org/10.1016/j.ijengsci.2006.06.005)
 31. Incropera FP, DeWitt DP (2001) *Fundamentals of heat and mass transfer*. Wiley, New York
 32. Ozalp AA (2006) A computational study to predict the combined effects of surface roughness and heat flux conditions on converging-nozzle flows. *Trans Can Soc Mech Eng* 29:67–80
 33. Wu JS, Tseng KC (2001) Analysis of micro-scale gas flows with pressure boundaries using direct simulation Monte Carlo method. *Comput Fluid* 30:711–735. doi:[10.1016/S0045-7930\(00\)00029-3](https://doi.org/10.1016/S0045-7930(00)00029-3)
 34. White FM (1988) *Fluid mechanics*. McGraw-Hill, Singapore
 35. Wang H, Wang Y, Zhang J (2005) Influence of ribbon structure rough wall on the microscale Poiseuille flow. *J Fluid Eng ASME Trans* 127:1140–1145. doi:[10.1115/1.2060733](https://doi.org/10.1115/1.2060733)
 36. Wu P, Little WA (1983) Measurement of friction factors for the flow of gases in very fine channels used for microminiature Joule–Thompson refrigerators. *Cryogenics* 23:273–277. doi:[10.1016/0011-2275\(83\)90150-9](https://doi.org/10.1016/0011-2275(83)90150-9)
 37. Kohl MJ, Abdel-Khalik SI, Jeter SM, Sadowski DL (2005) An experimental investigation of microchannel flow with internal pressure measurements. *Int J Heat Mass Transf* 48:1518–1533. doi:[10.1016/j.ijheatmasstransfer.2004.10.030](https://doi.org/10.1016/j.ijheatmasstransfer.2004.10.030)
 38. Choi SB, Barron RF, Warrington RO (1991) Fluid flow and heat transfer in microtubes. *Micromech Sens Actuators Syst* 32:123–134
 39. Yu D, Warrington R, Baron R, Ameel T (1995) An experimental and theoretical investigation of fluid flow and heat transfer in microtubes. *ASME/JSME Therm Eng Conf* 1:523–530
 40. Vijayalakshmi K, Anoop KB, Patel HE (2009) Effects of compressibility and transition to turbulence on flow through microchannels. *Int J Heat Mass Transf* 52:2196–2204. doi:[10.1016/j.ijheatmasstransfer.2008.07.056](https://doi.org/10.1016/j.ijheatmasstransfer.2008.07.056)
 41. Ozalp AA, Dincer I (2010) Hydrodynamic-thermal boundary layer development and mass transfer characteristics of a circular cylinder in confined flow. *Int J Therm Sci* 49:1799–1812. doi:[10.1016/j.ijthermalsci.2010.04.016](https://doi.org/10.1016/j.ijthermalsci.2010.04.016)
 42. Li J, Peterson GP, Cheng P (2004) Three-dimensional analysis of heat transfer in a micro-heat sink with single phase flow. *Int J Heat Mass Transf* 47:4215–4231. doi:[10.1016/j.ijheatmasstransfer.2004.04.018](https://doi.org/10.1016/j.ijheatmasstransfer.2004.04.018)